










Topological spin memory of antiferromagnetically coupled skyrmion pairs in Co/Gd/Pt multilayers

Xiao Wang ¹, Alexandra R. Stuart,² Mitchell S. Swyt,² Carla M. Quispe Flores,² Andy T. Clark ¹,
Adzo Fiagbenu,^{1,2} Rajesh V. Chopdekar ³, Pavel N. Lapa,⁴ Zhuyun Xiao ^{3,5}, Dava Keavney,⁶
Richard Rosenberg,⁶ Michael Vogel,⁴ John E. Pearson ⁴, Suzanne G. E. te Velthuis ⁴, Axel Hoffmann ^{4,7},
Kristen S. Buchanan ^{2,*} and Xuemei M. Cheng ^{1,†}

¹*Department of Physics, Bryn Mawr College, Bryn Mawr, Pennsylvania 19010, USA*

²*Department of Physics, Colorado State University, Fort Collins, Colorado 80523, USA*

³*Advance Light Source, Lawrence Berkeley National Laboratory, Berkeley, California 94720, USA*

⁴*Materials Science Division, Argonne National Laboratory, Lemont, Illinois 60439, USA*

⁵*Electrical and Computer Engineering, University of California, Los Angeles, California 90095, USA*

⁶*Advanced Photon Source, Argonne National Laboratory, Lemont, Illinois 60439, USA*

⁷*Department of Materials Science and Engineering, University of Illinois at Urbana-Champaign, Urbana, Illinois 61801, USA*



(Received 1 February 2022; revised 8 June 2022; accepted 29 July 2022; published 30 August 2022)

Antiferromagnetically (AFM) coupled skyrmions offer potential advantages for spintronic devices, including reduced dipolar fields that may enable smaller skyrmion sizes and a reduction of the skyrmion Hall effect. However, the topological stability of AFM-coupled skyrmions subjected to dramatic spin deformation through low-temperature cycling has not been investigated. Here we report the discovery of a topological spin memory effect for AFM-coupled skyrmion pairs in [Co/Gd/Pt]₁₀ multilayered films. Photoemission electron microscopy imaging shows that bubble skyrmions in the multilayer that are stable at room temperature evolve into complex in-plane spin textures as the temperature is lowered and reform completely when the sample is warmed back up. Simulations demonstrate that Dzyaloshinskii-Moriya interactions play a key role in this spin memory effect, and furthermore reveal that the topological charge is preserved throughout the dramatic spin texture rearrangement and recovery. These results highlight a key aspect of topological protection—the preservation of the topological properties under continuous deformation—and also provide a promising avenue for information encryption and recovery.

DOI: [10.1103/PhysRevMaterials.6.084412](https://doi.org/10.1103/PhysRevMaterials.6.084412)

I. INTRODUCTION

Magnetic skyrmions are small swirling spin textures with nontrivial topology that form in materials with broken symmetry and strong Dzyaloshinskii-Moriya interactions (DMIs) [1,2]. Multilayered materials with interfacial DMIs have enabled the formation of stable skyrmions at room temperature, usually bubble skyrmions consisting of small, typically circular cores surrounded by chiral Néel-type domain walls [3–7]. Strategies for creating skyrmions on demand have been described [4–6,8–14], and current driven skyrmion motion has been observed [3,4,10,13,14]. Recently, antiferromagnetically (AFM) coupled skyrmions [9,11,12] have attracted increasing interest because they offer potential advantages for spintronic devices, including lower dipolar fields that may enable smaller skyrmion sizes and a reduction of the skyrmion Hall effect. Since the skyrmion Hall effect is related to the gyromagnetic force on the skyrmion core, AFM-coupled skyrmions will experience opposite gyroscopic forces from the two sublattices that may cancel each other out, which

should reduce or even eliminate undesirable transverse motion [13,15–17]. Multilayered materials with antiferromagnetic interlayer exchange coupling are particularly attractive for applications because they offer a high degree of customization since the sublattice magnetizations and the g -factors can be tuned through the choice of materials and layer thicknesses. AFM-coupled skyrmions have been detected in Ruderman-Kittel-Kasuya-Yosida (RKKY)-coupled synthetic antiferromagnet multilayers [9,11]. However, the effect of temperature on the stability of AFM-coupled skyrmions has received limited attention, and the work done thus far has focused mainly on the stability of skyrmions in synthetic antiferromagnetic multilayers as a function of increasing temperature to confirm long-term stability for applications [9].

In addition to potential applications for spintronic devices, magnetic skyrmions are a model system for exploring the role of topology in materials and fundamental condensed-matter physics involving DMIs. Unlike the Heisenberg exchange interactions that favor collinear alignment, DMIs favor chiral twisting of the spins and promote a specific domain-wall chirality at the skyrmion boundary, which leads to a nontrivial topological charge for the skyrmion [18]. Because of their topology, magnetic skyrmions cannot be continuously deformed into a topologically trivial magnetic state, and they are

*kristen.buchanan@colostate.edu

†xcheng@brynmawr.edu

therefore better protected against annihilation as compared to topologically trivial spin textures [19]. While the role of topology in skyrmion annihilation has been investigated for ferromagnetic skyrmions [18–20], the limits of how far a skyrmion can be deformed and still recovered have not been explored in detail, and skyrmion deformation and recovery have not yet been investigated in AFM-coupled skyrmion pairs.

Here we report on the observation of the temperature-dependent spin texture evolution and the discovery of a topological spin memory effect in a [Co/Gd/Pt]₁₀ multilayer thin film. The [Co/Gd/Pt]₁₀ multilayer [21] is ideally suited for exploring topological protection in magnetically coupled skyrmion pairs. The broken symmetry, large interfacial DMIs, and perpendicular magnetic anisotropy from the Pt/Co interfaces favor skyrmion formation in the Co layer [22–24], and the strong antiferromagnetic exchange coupling between the Co and Gd layers promotes the formation of AFM-coupled skyrmion pairs [14,25–27]. Furthermore, the Gd moment increases substantially with decreasing temperature [21,28–30], hence temperature (T) can be used to continuously tune the magnetic parameters of the multilayer. Temperature-dependent photoemission electron microscopy (PEEM) imaging, which was used to image the Co and Gd layers in the top repeat of the multilayer, shows that stable AFM-coupled bubble skyrmion pairs at room temperature deform dramatically into complex in-plane spin textures, and the original bubbles are no longer visible when the [Co/Gd/Pt]₁₀ multilayer undergoes a spin reorientation transition (SRT) with decreasing temperature, but the original bubble skyrmions reform completely as the temperature is subsequently increased back. The observed complete recovery of bubble skyrmions after dramatic spin deformation is referred to as the topological spin memory effect. Micromagnetic simulations highlight the role of DMI and topology in this spin memory effect.

II. EXPERIMENTAL AND NUMERICAL METHODS

A. Film deposition, characterization, and skyrmion preparation

The evolution of AFM-coupled skyrmions [Fig. 1(a)] under a continuous deformation was investigated in sputter-deposited multilayers of [Co (0.5 nm)/Gd (1 nm)/Pt (1 nm)]₁₀ with a Ta (5 nm)/Pt (4 nm) buffer layer and an Al (2 nm) capping layer, illustrated in Fig. 1(b) and referred to as [Co/Gd/Pt]₁₀. The multilayers were sputter-deposited onto a Si substrate with a 300-nm-thick thermally oxidized SiO₂ top layer. The base pressure was 5×10^{-8} Torr and the deposition pressure was 5 mTorr of Ar gas with a flow rate of 30 SCCM. X-ray diffraction and reflectometry measurements were performed to confirm the composition and periodicity of the multilayer films. Magnetization versus temperature and magnetic hysteresis measurements were made at selected temperatures using a SQUID magnetometer to determine the saturation magnetization, magnetic anisotropy, and interlayer exchange parameters.

The DMI was measured for a (Ta/Pt/[Co/Gd/Pt]) single repeat sample with the same thicknesses used for the [Co/Gd/Pt]₁₀ multilayer by Brillouin light scattering (BLS) in a backscattering configuration [Fig. 1(f), inset] with a

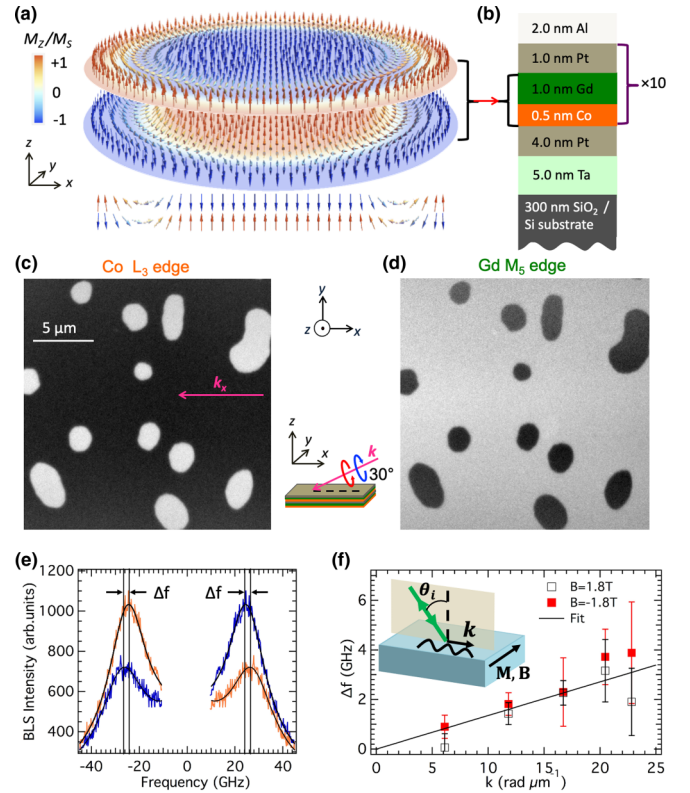


FIG. 1. (a) Illustration of an AFM-coupled bubble skyrmion pair, with perspective (top) and cross-sectional views (bottom). Arrows represent the atomic spins, and the color represents the z -component of the magnetization. The topological charge Q of the top (bottom) skyrmion is $+1$ (-1). (b) Schematic structure of the sputtered [Co/Gd/Pt]₁₀ multilayer film. (c), (d) XMCD-PEEM images acquired at the Co L_3 (c) and Gd M_5 (d) absorption edges at remanence and room temperature where the x-rays are incident in the $-x$ direction, 30° away from the film plane, as illustrated by the x-ray wave vector \mathbf{k} in (c). The [Co/Gd/Pt]₁₀ film exhibits perpendicular anisotropy at room temperature, hence the spins in the bright and dark regions are along the $-z$ and $+z$ directions, respectively, indicating that the magnetic bubbles observed in the Co and Gd layers are AFM-coupled. (e) Room-temperature BLS measurements of a Ta/Pt/[Co/Gd/Pt] film at $k = 16.7 \text{ rad } \mu\text{m}^{-1}$ with an in-plane field of $B = 1.8 \text{ T}$ show a frequency shift Δf between the Stokes and anti-Stokes surface spin wave peaks where the red (blue) are the raw (reversed) spectra. Lorentzian fit lines are overlaid. (f) Δf vs k for the Ta/Pt/[Co/Gd/Pt] film and a linear fit that corresponds to $D = 1.4 \text{ mJ m}^{-2}$. The inset of (f) shows a diagram of the BLS scattering configuration.

wavelength of 532 nm using a six-pass high contrast tandem Fabry-Pérot interferometer. The sample used for the BLS measurements was deposited under the same conditions as the [Co/Gd/Pt]₁₀ multilayer and capped with a 20-nm-thick layer of SiO₂ instead of Al. The spin-wave wave vector k is given by $k = 2k_o \sin \theta_i$, where k_o is the wave vector of the incident light and θ_i is the angle of incidence. The magnitude of the DMI D is obtained using $\Delta f = [2|\gamma|D/(\pi M_s)]k$ [31–34], where k is the wave vector of the measured spin waves, γ is the gyromagnetic ratio, and M_s is the saturation magnetization value of the Co layer. This approach for obtaining D was developed

for a single magnetic layer, whereas in the measured sample both the Co and Gd are magnetic and exchange coupled to one another. We estimate that neglecting the Gd in the analysis, which has a small moment at room temperature, has a $<3\%$ effect on the value obtained for D [see the Supplemental Material (SM) for details [35]].

Prior to the x-ray magnetic circular dichroism (XMCD) measurements and photoemission electron microscopy (PEEM) imaging, as described in more detail in the next sections, the samples were prepared to the skyrmion state using a room-temperature field treatment procedure by applying an in-plane magnetic field of 0.6 T and then turning it off. Polar magneto-optical Kerr effect (p-MOKE) imaging was used to confirm the presence of bubble skyrmions.

B. Photoemission electron microscopy

PEEM imaging of the [Co/Gd/Pt]₁₀ sample, which was field-treated to the skyrmion state, was conducted at magnetic remanence, i.e., zero magnetic field as a function of temperature, from room temperature to 33 K and back, at beamline 11.0.1 of the Advanced Light Source at Lawrence Berkeley National Laboratory. Element-specific images were obtained by tuning the x-ray energy to the Gd M_5 (1188.8 eV) and the Co L_3 (778.5 eV) edges. XMCD-PEEM images with a field of view of $20 \mu\text{m} \times 20 \mu\text{m}$ were obtained by taking the difference of a pair of images acquired with left- and right-circularly polarized x-rays to obtain the magnetic contrast. The brightness of the XMCD-PEEM images is proportional to the dot product of the magnetization \mathbf{M} and the x-ray propagation direction \hat{k} [36–38], i.e., the contrast is $c_{\text{PEEM}} : \mathbf{M} \cdot \hat{k} = M_x \cos(30^\circ) + M_z \sin(30^\circ)$, where the x-ray incident angle is 30° with respect to the sample plane. PEEM images, which are formed by secondary electrons that escape from the sample surface (~ 5 nm depth [39]), provide information about the spin configuration of the topmost Gd and Co layers in the sample.

C. X-ray magnetic circular dichroism spectroscopy

XMCD spectra were measured at magnetic remanence (zero magnetic field) with the sample field-treated to set it into the skyrmion state at beamline 4-ID-C of the Advanced Photon Source at Argonne National Laboratory. The temperature was cycled from room temperature to 10 K and back, and at each temperature XMCD spectra were obtained by taking the difference of a pair of x-ray absorption (XAS) spectra acquired using left- and right-circularly polarized x-rays with the energy tuned to the Co $L_{2,3}$ edges (765–810 eV) and the Gd $M_{4,5}$ edges (1170–1235 eV). The x-ray beam was set at 15° and 65° away from the sample plane, and the in-plane and out-of-plane components for the average remanent magnetic moments per atom for the Gd and Co layers (M_{Gd} and M_{Co}) were calculated at each temperature by applying the sum rules [37,38,40,41] (see the SM for details [35]). The x-ray beam was approximately $150 \mu\text{m}$ in diameter, hence the illuminated area of the sample is large compared to the size of individual bubble skyrmions, and the magnetization calculated from the XMCD measurements is averaged over a volume determined

by the x-ray illumination area and the electron escape depth (~ 5 nm [39]).

D. Micromagnetic simulations

Micromagnetic simulations were conducted using Mumax³ [42] to study the spin evolution as a function of temperature, where the material parameters were set to values appropriate for 170 K, followed by 50 K, then 30 K, and then back. This cycle was repeated a total of three times, and the relaxed state was calculated for each parameter set. The effects of the temperature were captured by varying the saturation magnetizations M_s of the Co and Gd as well as the interlayer exchange coupling, where the magnetization of the Gd undergoes by far the largest change. The saturation magnetization values for the Gd and Co were obtained from fits to magnetization versus temperature measurements (the M_s values for Gd are 3.25, 10.8, and $12.9 \times 10^5 \text{ A m}^{-1}$ for 170, 50, and 30 K, respectively, and the corresponding values for Co are 11.9, 13.4, and $13.6 \times 10^5 \text{ A m}^{-1}$), and the interlayer exchange and anisotropy were determined from fits to the magnetic hysteresis loops as well as consistency with the PEEM and XMCD measurements (see the SM for details [35]). The magnetization of the Gd increases with decreasing temperature, which leads to an increase in the shape anisotropy that is accounted for through the demagnetization energy. The intralayer exchange parameters (20×10^{-12} and $5 \times 10^{-12} \text{ J m}^{-1}$ for Co and Gd, respectively) and the Co anisotropy ($K_u = 1.6 \times 10^6 \text{ J m}^{-3}$) were held fixed, and the interlayer exchange across the Pt layer and the anisotropy parameter for the Gd layers were set to zero. The interlayer Co/Gd exchange was set to -0.177 , -0.708 , and -0.767 mJ m^{-2} for 170, 50, and 30 K, respectively. Two [Co/Gd/Pt] units were modeled using $2 \times 2 \text{ nm}^2$ cells with a thickness of 0.5 nm, and periodic boundary conditions were used in the out-of-plane (z) direction to represent the 10-repeat stack, and in the in-plane direction to better approximate an extended film.

Simulations were conducted with interfacial DMI values of 0, 1.5, and 2.5 mJ m^{-2} , assigned to the Co layer and held constant for all temperatures. (Note that negative values for D were used in the simulations, and for simplicity the magnitude of D is given. The sign of the DMI influences only the chirality of the Néel wall.) Effective interfacial DMI values of 1.5 mJ m^{-2} or larger are reasonable for Co/Pt, and values of $\geq 2.5 \text{ mJ m}^{-2}$ are possible for a 0.5-nm-thick Co film based on scaling published DMI measurements for Co/Pt by the Co thickness [22,23,43]. The Co/Gd interface is not expected to contribute appreciably to the DMI since DMI has not been observed for a transition-metal/rare-earth interface thus far, an assumption also made in previous work on Co/Gd [44]. Our measurements of D for (Ta/Pt/[Co/Gd/Pt]) with a 0.5-nm-thick Co layer fall within this range [Fig. 1(f)].

III. THE TOPOLOGICAL SPIN MEMORY EFFECT

A. AFM-coupled skyrmions at room temperature

PEEM imaging was used to study the evolution of AFM-coupled skyrmions in the [Co/Gd/Pt]₁₀ multilayer as a function of temperature. Element-specific, XMCD-based

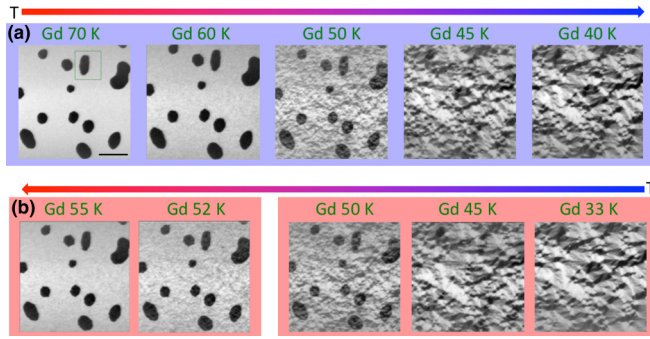


FIG. 2. Representative XMCD-PEEM images taken at remanence at the Gd M_5 edge as the temperature was (a) decreased from room temperature to 33 K and then (b) increased back (from right to left). A 5- μm -long scale bar that applies to all of the PEEM images is shown in the first image, and a green box in the same image indicates the skyrmion highlighted in Fig. 4. The sample was subjected to additional cooling and rewarming between the 50 and 52 K images in (b), shown in additional detail in the SM [35]. The PEEM images show that bubble skyrmions transition to a complex multidomain configuration on cooling down and reform when warming back up.

PEEM images taken at room temperature at the Co L_3 edge [Fig. 1(c)] and the Gd M_5 edge [Fig. 1(d)] show bubble skyrmions in the Co and Gd layers that are AFM-coupled. Since the spins are predominantly out-of-plane at room temperature in the $[\text{Co}/\text{Gd}/\text{Pt}]_{10}$ multilayer, as evidenced by XMCD ($M_x \approx 0$) and magnetometry measurements [see Figs. 3(a)–3(d) and 3(e)], the dark and bright areas in Figs. 1(c) and 1(d) correspond to regions with the magnetization in the $+z$ and $-z$ directions, respectively. Therefore, the bright areas in the Co layer and the dark areas in the Gd layer are the core areas of bubble skyrmion pairs, and the bright/dark contrast shows that each skyrmion core in the Co layer is mirrored in the Gd layer with corresponding spins antiferromagnetically aligned. We use the term “AFM-coupled skyrmions” to refer to these mirrored skyrmions where the coupling is due to the exchange coupling between the Co and Gd layers. It is important to note that apart from the compensation temperature (approximately 110 K for this multilayer; see the SM for fits to the magnetometry data [35]), the AFM-coupled skyrmions are ferrimagnetic since the net moment is nonzero.

We refer to the spin states in Fig. 1 as bubble skyrmions. Although the imaging resolution of approximately 30 nm is not sufficient to resolve the domain-wall structure, the domain walls at the bubble skyrmion boundaries are expected to be Néel-type based on previous work [11] and micromagnetic simulations using the DMI value from the BLS measurements [Figs. 1(e) and 1(f)]. As shown in Fig. 1(e), room-temperature BLS measurements of surface spin waves in a single repeat sample ($\text{Ta}/\text{Pt}/[\text{Co}/\text{Gd}/\text{Pt}]$) show a sizable frequency shift Δf for surface spin waves traveling in opposite directions. The magnitude of the effective interfacial DMI, D (the value used in micromagnetic simulations), is obtained from the data shown in Fig. 1(f) using a weighted least-squares fit to $\Delta f = [2|\gamma|D/(\pi M_s)]k$ [31–34] with $M_s = 1.18 \pm 0.25 \text{ MA m}^{-1}$, the room-temperature value for the saturation magnetization of the Co layer obtained from XMCD measurements

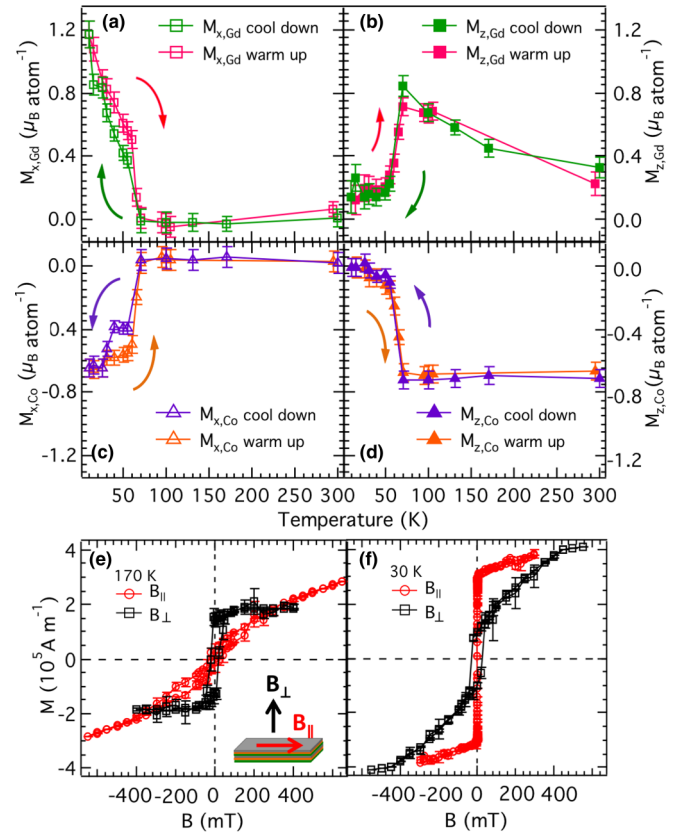


FIG. 3. Temperature-dependent in-plane and out-of-plane magnetization components for the Gd (a), (b) and Co (c), (d) layers calculated from the XMCD spectra taken as the temperature was cycled from 300 to 10 K and back at remanence with the sample in the skyrmion state. The lines are a guide to the eye, and the curved arrows indicate the direction of the temperature change. (e), (f) Magnetic hysteresis loops with the magnetic field applied parallel (B_{\parallel}) to and normal (B_{\perp}) to the sample plane measured by a SQUID magnetometer show that the magnetic easy axis is out-of-plane at 170 K (e) and in-plane at 30 K (f).

made with a saturating magnetic field, and $|\gamma|/2\pi = 28.0 \text{ rad GHz T}^{-1}$. This yields an effective interfacial DMI value of $D = 1.4 \pm 0.3 \text{ mJ m}^{-2}$, which is large enough to favor the formation of Néel-type skyrmions. The error bars for Δf in Fig. 1(f) increase with increasing k and are large for $k = 22.8 \mu\text{m}^{-1}$. The larger uncertainty at large k results from a combination of increased background from entropy scattering due to impurities, increased linewidth of the surface spin wave signal (full width at half-maximum values are 22–24 GHz for $k = 22.8 \mu\text{m}^{-1}$), and a lower magnon-photon scattering efficiency that results in a lower signal-to-noise ratio.

B. Observation of the spin memory effect

Temperature-dependent PEEM images and XMCD spectra were obtained while cooling the $[\text{Co}/\text{Gd}/\text{Pt}]_{10}$ film from room temperature in zero magnetic field starting from the skyrmion state down to 33 and 10 K, respectively, and then warming it back up. The PEEM images reveal a spin memory effect when the temperature is cycled. On cooling down [Fig. 2(a)] the bubble skyrmions first remain the same from

room temperature [see Fig. 1(d)] to 70 K. As T is decreased from 70 K down to 45 K, complex spin texture patterns appear in the PEEM images and gradually strengthen, while the bubble cores fade. These PEEM image changes coincide with an increase in the in-plane remanent magnetization [Figs. 3(a) and 3(c)] and a sharp drop of the out-of-plane remanent magnetization magnitudes [Figs. 3(b) and 3(d)]. As T is further reduced, the bubble skyrmions continue to fade until they are no longer visible and the spin state becomes a complex multidomain state. When T is subsequently increased (Fig. 2), bubble skyrmions reappear and, surprisingly, the reformed bubble skyrmions have almost exactly the same locations, sizes, and shapes as the original bubbles, in spite of the fact that the spin textures at low T are completely different.

Temperature-dependent XMCD spectra and magnetometry measurements of the $[\text{Co}/\text{Gd}/\text{Pt}]_{10}$ films (Fig. 3) show that the temperature range at which the bubble skyrmion state transitions to the multidomain state coincides with a spin reorientation transition. The XMCD results in Figs. 3(a) and 3(c) show that as temperature T is decreased, the magnitudes of the in-plane remanent magnetization for the Gd ($|M_{\text{Gd}, x}|$) and the Co ($|M_{\text{Co}, x}|$) layers both remain at zero until 70 K and then increase to $1.17 \pm 0.06 \mu_{\text{B}} \text{ atom}^{-1}$ and $0.65 \pm 0.07 \mu_{\text{B}} \text{ atom}^{-1}$ at 10 K, respectively. These increases in the in-plane magnetization are accompanied by a drop in the magnitudes of the out-of-plane remanent magnetizations for Gd ($|M_{\text{Gd}, z}|$) and Co ($|M_{\text{Co}, z}|$) as shown in Figs. 3(b) and 3(d), which is indicative of a spin reorientation transition from out-of-plane to in-plane. Based on Figs. 3(a)–3(d), we define the onset temperature for the SRT as $T_{\text{SRT}} = 70$ K. Magnetometry measurements at 170 K [Fig. 3(e)] and 30 K [Fig. 3(f)] further confirm that the $[\text{Co}/\text{Gd}/\text{Pt}]_{10}$ multilayer exhibits perpendicular magnetic anisotropy when $T > T_{\text{SRT}}$, and in-plane anisotropy when $T < T_{\text{SRT}}$.

It is also worth noting that as T is decreased from 300 to 70 K [Fig. 3(b)], $|M_{\text{Gd}, z}|$ increases from $0.33 \pm 0.07 \mu_{\text{B}} \text{ atom}^{-1}$ to $0.84 \pm 0.06 \mu_{\text{B}} \text{ atom}^{-1}$. At 70 K, $|M_{\text{Gd}, z}| > |M_{\text{Co}, z}|$, so the shape anisotropy in the Gd layer that favors an in-plane magnetic configuration becomes more important, which causes the Gd spins and consequently the Co spins to rotate into the plane, and the spin reorientation transition begins. Our results are consistent with the reported complex temperature-dependent magnetic behavior of the Gd layer [21,28–30]. The spin reorientation transition occurs due to competition between the shape anisotropies of the two magnetic layers and the interfacial anisotropy at the Co/Pt interfaces [45,46], and the temperature can be tuned based on the Co and Gd thicknesses. Similar spin reorientations have been reported previously, for example in Gd/Fe and Gd/FeCo multilayers [47,48]. In addition, the measured M_{Gd} and M_{Co} have opposite signs, as expected for antiferromagnetic coupling.

C. The role of DMI and topological protection

To gain insight into the evolution of the spin textures through the spin reorientation transition, we compare the experimental images to micromagnetic simulations of a single bubble skyrmion in Fig. 4. The simulations in Figs. 4(c)–4(f), performed with $D = 2.5 \text{ mJ m}^{-2}$, show a bubble skyrmion at 170 K [$T > T_{\text{SRT}}$, Fig. 4(c)] and a patchwork pattern in

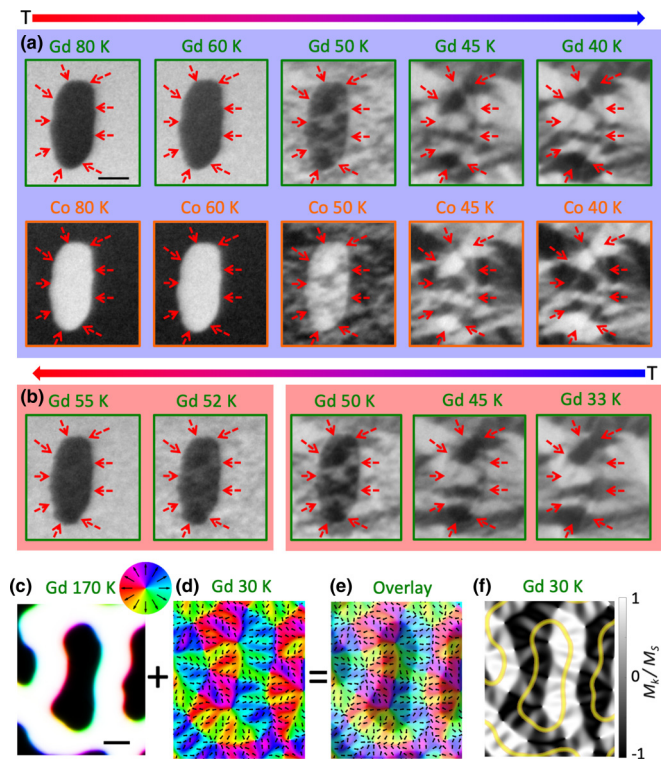


FIG. 4. (a), (b) Zoomed-in PEEM images of a selected region [marked in Fig. 2(a)] are shown as T is decreased from room temperature to 33 K (a) and subsequently increased back [(b), right to left]. The opposite contrast for the Co and Gd layers indicates that the layers are AFM-coupled. The dashed red arrows highlight the bubble skyrmion boundary at 80 K, and the scale bar in (a) is $1 \mu\text{m}$. (c)–(f) Zoomed-in simulated images of the Gd spin configuration in a selected region [marked in Fig. 5(r)] at temperatures above and below T_{SRT} . A 200-nm-long scale bar for (c)–(f) is shown at the bottom of (c). In (c) and (d), the brightness corresponds to the out-of-plane magnetization M_z , and the colors show the in-plane magnetization angle as illustrated by the color wheel. A bubble skyrmion with a chiral Néel domain wall for $T > T_{\text{SRT}}$ (c) evolves into two radial vortices and an antivortex (d) as the temperature is lowered below T_{SRT} . (e) An overlay of (c) and (d) shows that the chirality of the skyrmion domain wall is preserved in the in-plane spin distribution. (f) Simulated PEEM image of the spin configuration at 30 K (d) where the gray level represents the normalized magnetization component along the x-ray propagation direction. The yellow lines show the boundaries of the simulated bubble skyrmions at 170 K.

the simulated PEEM image at 30 K [$T < T_{\text{SRT}}$, Fig. 4(f)], both of which agree reasonably well with the experimental PEEM images in Figs. 4(a) and 4(b). Simulations conducted with $D = 1.5 \text{ mJ m}^{-2}$ show similar behavior. The simulated PEEM image for the out-of-plane state is almost identical to the magnetization contrast in Fig. 4(a) and hence is not shown. The contrast of the simulated PEEM image of the in-plane state at 30 K [Fig. 4(f)] is largely dark on the left side and bright on the right, whereas in the experimental PEEM images the contrast for the in-plane distributions is more varied. This could be due to the smaller size of the simulated bubble skyrmion as compared to the experimental skyrmions, and we note that coupling between unit repeats can also lead to

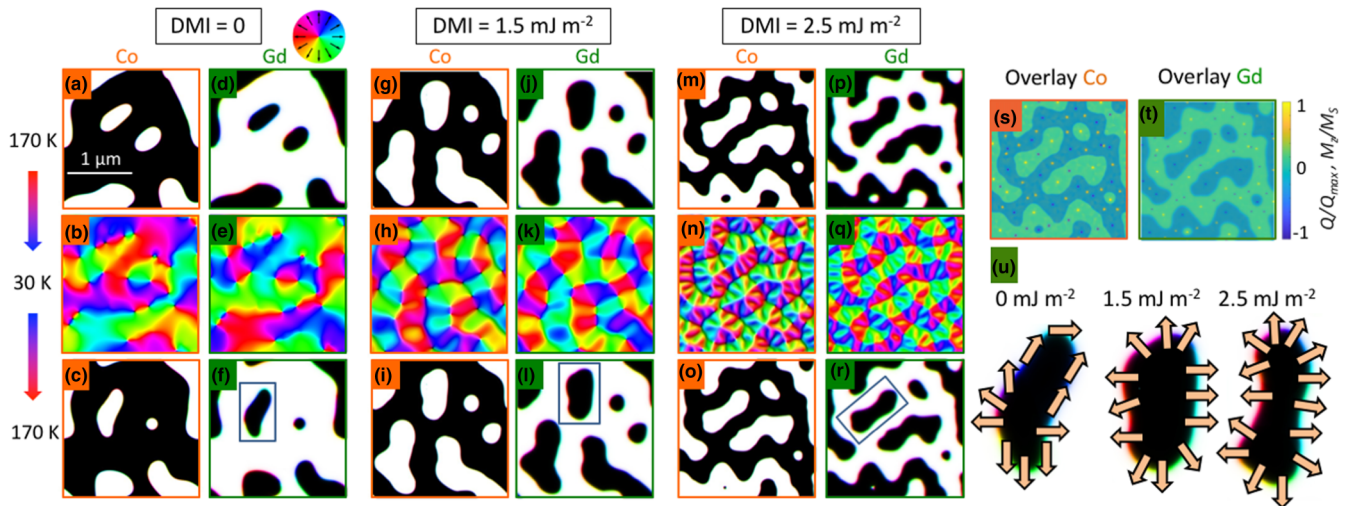


FIG. 5. Simulations of the spin texture evolution of the Co and Gd layers are shown in the top (orange boxes) and bottom (green boxes) rows, respectively, for DMI values of 0 mJ m^{-2} (a)–(f), 1.5 mJ m^{-2} (g)–(l), and 2.5 mJ m^{-2} (m)–(r). The relaxed spin states are shown for parameters appropriate for 170 K (a,d,g,j,m,p), then after changing to parameters for 30 K (b,e,h,k,n,q), followed by a return to the 170 K parameters (c,f,i,l,o,r). The scale bar in (a) is $1 \mu\text{m}$. The brightness corresponds to M_z , and the colors show the in-plane angle (see the color wheel). Overlays (s,t) for the Co and Gd, respectively, are of the topological charge density of the in-plane state at 30 K (small light and dark dots that are found at the radial vortex and antivortex cores) and M_z of the skyrmions at 170 K, which is shown as fainter yellow-blue contrast that matches the white-black contrast in (m,p), respectively. The net topological charge Q at 30 K within the region of each of the 170 K bubble skyrmions is $+1/2$ for the Co (s) and $-1/2$ for the Gd layer (t), which is half of the Q of the corresponding skyrmion. Part (u) shows the zoomed images of the skyrmions in the boxes in (f), (l), and (r), where the arrows show the magnetization directions within the domain walls.

increased complexity in the in-plane distributions (see the SM [35]). The corresponding full-view simulation results for the Co and Gd layers in Figs. 5(m)–5(o) and Figs. 5(p)–5(r), respectively, show AFM-coupled skyrmions with opposite contrast and a spin texture evolution with T that is consistent with the experimental PEEM results in Fig. 2.

The micromagnetic simulations not only resemble the experimental PEEM results, but they also help to provide insight into the reason for the observed spin memory effect. The large bubble skyrmions found above T_{SRT} [Fig. 4(c)] evolve into a complex in-plane magnetization configuration at 30 K [Fig. 4(d)] that involves multiple magnetic antivortices and radial vortices. The tiny cores ($\sim 10 \text{ nm}$) of these radial vortices and antivortices remain out-of-plane and can be more clearly seen as dots in Figs. 5(s) and 5(t) that show topological charge densities of opposite signs concentrated at the cores of the radial vortices and antivortices. More importantly, Fig. 4(e), an overlay of Figs. 4(c) and 4(d), shows that the spin configuration of the Néel domain wall near the bubble skyrmion edge at 170 K is similar to the in-plane spin directions within the corresponding region at 30 K. The overlay image shows that the memory of the topological information is imprinted into the in-plane state as the temperature is reduced across the spin reorientation transition in two ways: the polarizations of the antivortex and radial vortex cores preserve the memory of the out-of-plane direction of the skyrmion cores, and the chirality of the skyrmion domain wall expands and forms the basis of the bodies of antivortices and radial vortices. The imprinted chirality, in turn, facilitates the reformation of the skyrmion during the subsequent warm-up since the DMI combined with the preserved skyrmion core directions favor the original chirality and hence the formation of a skyrmion

that is the same as the original. In the absence of DMI, the reformation process should be stochastic.

Moreover, overlay images of the topological charge density of the in-plane state at 30 K and the magnetization profiles of the bubble skyrmion state at 170 K, Figs. 5(s) and 5(t), reveal that the net topological charge Q of the in-plane spin textures at 30 K found within the region of any given bubble skyrmion at 170 K is half of the Q of the original skyrmion. For example, the Gd skyrmion in Fig. 4(c) changes to two radial vortices and an antivortex in the in-plane configuration at 30 K as shown in Figs. 4(d) and 5(t). The net Q at 30 K is $-1/2$, equal to half of the Q of the original Gd skyrmion at 170 K. For a bubble skyrmion, $Q = +1$ or -1 and the topological charge resides in the vicinity of the chiral domain wall. If Q is preserved during the SRT, half of it would be expected to move inwards, and the other half should move outwards with respect to the original skyrmion boundary as the chiral domain wall expands. The observed Q of $\pm 1/2$ at low temperatures within each of the original skyrmion boundaries is hence a strong indication that Q is preserved across the spin reorientation transition.

Simulation results for three different DMI values—0, 1.5, and 2.5 mJ m^{-2} —are compared in Fig. 5. In the absence of DMI, bubblelike domain patterns also appear for $T > T_{\text{SRT}}$, but these are topologically trivial bubbles [compare the images in Fig. 5(u)] that form due to the dipolar interactions in materials with perpendicular magnetic anisotropy. Moreover, the domain patterns after temperature cycling bear little resemblance to the original high- T spin distributions with no DMI. In contrast, for $D = 1.5$ and 2.5 mJ m^{-2} , Q is preserved through the spin reorientation transition, and bubble skyrmions with the original Q are recovered.

IV. DISCUSSION

Our simulation results suggest that the experimentally observed spin memory effect is mainly due to the interfacial DMI in the $[\text{Co}/\text{Gd}/\text{Pt}]_{10}$ film and the resultant topological protection it offers. The Néel domain walls and the bubble skyrmion cores at high temperatures set the directions of the in-plane distributions and the net core polarizations (see the SM [35]), respectively, of the radial vortices and antivortices in the in-plane magnetic configurations at $T < T_{\text{SRT}}$ and, since the DMI favors a particular Néel wall chirality, the skyrmions will reform at similar locations and with a similar shape when the sample is warmed back above T_{SRT} . The qualitative similarities between the simulations and the experimental PEEM images strongly suggest that the chirality preservation mechanism seen in the simulations drives the experimentally observed skyrmion recovery. The skyrmion sizes and shapes do not match as perfectly as they do in the experiments before and after the temperature cycling, which suggests that pinning due to variations in the magnetic properties of the film may also contribute. However, the complete disappearance of the bubble skyrmion cores in the PEEM images at low temperatures suggests that even if pinning is present, it is unlikely to explain the spin memory effect on its own. We note that the simulated bubble skyrmions are smaller in comparison to the experiments, which is likely due to the limited area considered in the simulations. Nevertheless, the simulation results with DMI values of 1.5 and 2.5 mJ m^{-2} , a range that overlaps with the value of $1.4 \pm 0.3 \text{ mJ m}^{-2}$ obtained by BLS for the $(\text{Ta}/\text{Pt}/[\text{Co}/\text{Gd}/\text{Pt}])$ multilayer, show strong qualitative agreement with the experiment, which suggests that the interfacial DMI and the nontrivial skyrmion topologies allow for dramatic rearrangement and recovery of the bubble skyrmion state in AFM-coupled skyrmion pairs. The simulations show that the spin memory effect occurs for a broad range of experimentally realizable DMI values, hence there are opportunities to further optimize materials for current-driven motion and transition temperatures while still realizing the spin memory effect.

The experimental PEEM images in Figs. 4(a) and 4(b) show in-plane spin distributions at low temperatures with a high degree of complexity. The simulations show that there are more antivortex and radial vortex cores inside the larger bubble skyrmions and consequently a higher degree of in-plane complexity at low temperatures as compared to what is observed for smaller skyrmions [Figs. 5(m)–5(t)]. This trend is likely to continue with increasing skyrmion size since the DMI favors noncollinear spin textures. The coupling between repeat units—dipolar and exchange—can also affect the complexity of the in-plane state. With nonzero exchange coupling across the Pt, simpler in-plane spin textures are obtained for small skyrmions (see the SM [35]), whereas the more complex in-plane distributions within a single skyrmion region that are shown in Figs. 4(d) and 4(f) arise because of the stray fields from skyrmions with a slightly different layout in another $[\text{Co}/\text{Gd}/\text{Pt}]$ repeat unit, which occurs in the simulations when the exchange across the Pt is set to zero. The experimental PEEM images in Figs. 2 and 4 are sensitive to the topmost Co and Gd layers, so they do not provide any information about whether the repeat units are coupled or

not. Regardless of the complexity of the in-plane distributions and the presence or absence of exchange coupling across the Pt, the spin states along the domain walls of the original skyrmions are preserved through the temperature cycling, and the skyrmions are recovered when DMI is included in the simulations.

V. CONCLUSION

In conclusion, we have discovered a topological spin memory effect in $[\text{Co}/\text{Gd}/\text{Pt}]_{10}$ multilayers that stems from the robust nontrivial topology of magnetic skyrmions. AFM-coupled skyrmion pairs that are stable at room temperature are recovered when the film is warmed up despite the previous transition to dramatically different in-plane spin textures on cooling down. The spin textures are deformed continuously as the temperature is changed since the $[\text{Co}/\text{Gd}/\text{Pt}]_{10}$ multilayers undergo a spin reorientation transition from out-of-plane at high temperatures ($T > T_{\text{SRT}} = 70 \text{ K}$) to in-plane at low temperatures ($T < T_{\text{SRT}}$), as shown by temperature-dependent XMCD spectra and magnetometry measurements. PEEM images show that the bubble skyrmions deform dramatically into collections of radial vortices and antivortices and then reform almost perfectly when the temperature is cycled back above T_{SRT} . A comparison of PEEM images with micromagnetic simulations suggests that the chiralities of the bubble skyrmion domain walls are encoded in the in-plane spin distributions below T_{SRT} , and that this encoding, because of the presence of DMI, leads to the reformation of bubble skyrmions with remarkably similar shapes, sizes, and locations when the temperature is raised back above T_{SRT} . Our results highlight the robust nature of the topological protection associated with skyrmion spin textures and the DMI. Additionally, the observed AFM-coupled bubble skyrmion pairs are stable over a large temperature range from room temperature down to 70 K without any external magnetic field, a temperature range that includes the angular momentum compensation temperature (about 125 K for the $[\text{Co}/\text{Gd}/\text{Pt}]_{10}$ multilayer used in this work), hence they may be useful for skyrmion-based spintronic applications. More importantly, these results demonstrate a topological spin memory effect that, while discovered and demonstrated using AFM-coupled skyrmion pairs, should be realizable with any topological spin texture. The spin memory effect provides a means to encrypt and recover spin information that has strong potential to serve as the basis for a magnetic analog of invisible ink, and it may also inspire new approaches to controlled skyrmion formation and manipulation for logic applications.

ACKNOWLEDGMENTS

Work at BMC and CSU is supported by the National Science Foundation (DMR Grants No. 1708790 and No. 1709525). Work at the Materials Science Division of Argonne National Laboratory (film deposition, XRR, and p-MOKE imaging) is supported by U.S. Department of Energy, Office of Science, Basic Energy Sciences, Materials Sciences and Engineering Division. We used the Advanced Photon Source at ANL (XMCD) and the Advanced Light Source at LBNL (PEEM), which are DOE Office of Science User

Facilities under Contracts No. DE-AC02-06CH11357 and No. DE-AC02-05CH11231, respectively. We also used character-

ization facilities at the Colorado State University Analytical Resources Core Facility, RRID:SCR_021758.

- [1] I. Dzyaloshinsky, A thermodynamic theory of “weak” ferromagnetism of antiferromagnetics, *J. Phys. Chem. Solids* **4**, 241 (1958).
- [2] T. Moriya, Anisotropic superexchange interaction and weak ferromagnetism, *Phys. Rev.* **120**, 91 (1960).
- [3] S. Woo, K. Litzius, B. Krüger, M. Y. Im, L. Caretta, K. Richter, M. Mann, A. Krone, R. M. Reeve, M. Weigand, P. Agrawal, I. Lemesh, M. A. Mawass, P. Fischer, M. Kläui, and G. S. Beach, Observation of room-temperature magnetic skyrmions and their current-driven dynamics in ultrathin metallic ferromagnets, *Nat. Mater.* **15**, 501 (2016).
- [4] W. Jiang, P. Upadhyaya, W. Zhang, G. Yu, M. B. Jungfleisch, F. Y. Fradin, J. E. Pearson, Y. Tserkovnyak, K. L. Wang, O. Heinonen, S. G. E. te Velthuis, and A. Hoffmann, Blowing magnetic skyrmion bubbles, *Science* **349**, 283 (2015).
- [5] O. Boulle, J. Vogel, H. Yang, S. Pizzini, D. De Souza Chaves, A. Locatelli, T. O. Menteş, A. Sala, L. D. Buda-Prejbeanu, O. Klein, M. Belmeguenai, Y. Roussigné, A. Stashkevich, S. Mourad Chérif, L. Aballe, M. Foerster, M. Chshiev, S. Auffret, I. M. Miron, and G. Gaudin, Room-temperature chiral magnetic skyrmions in ultrathin magnetic nanostructures, *Nat. Nanotechnol.* **11**, 449 (2016).
- [6] D. A. Gilbert, B. B. Maranville, A. L. Balk, B. J. Kirby, P. Fischer, D. T. Pierce, J. Unguris, J. A. Borchers, and K. Liu, Realization of ground-state artificial skyrmion lattices at room temperature, *Nat. Commun.* **6**, 8462 (2015).
- [7] M. He, G. Li, Z. Zhu, Y. Zhang, L. Peng, R. Li, J. Li, H. Wei, T. Zhao, X. G. Zhang, S. Wang, S. Z. Lin, L. Gu, G. Yu, J. W. Cai, and B. G. Shen, Evolution of topological skyrmions across the spin reorientation transition in Pt/Co/Ta multilayers, *Phys. Rev. B* **97**, 174419 (2018).
- [8] Z. Wang, X. Zhang, J. Xia, L. Zhao, K. Wu, G. Yu, K. L. Wang, X. Liu, S. G. E. te Velthuis, A. Hoffmann, Y. Zhou, and W. Jiang, Generation and Hall effect of skyrmions enabled using nonmagnetic point contacts, *Phys. Rev. B* **100**, 184426 (2019).
- [9] W. Legrand, D. Maccariello, F. Ajejas, S. Collin, A. Vecchiola, K. Bouzehouane, N. Reyren, V. Cros, and A. Fert, Room-temperature stabilization of antiferromagnetic skyrmions in synthetic antiferromagnets, *Nat. Mater.* **19**, 34 (2020).
- [10] W. Legrand, D. Maccariello, N. Reyren, K. Garcia, C. Moutafis, C. Moreau-Luchaire, S. Collin, K. Bouzehouane, V. Cros, and A. Fert, Room-Temperature Current-Induced Generation and Motion of sub-100 nm Skyrmions, *Nano Lett.* **17**, 2703 (2017).
- [11] T. Dohi, S. DuttaGupta, S. Fukami, and H. Ohno, Formation and current-induced motion of synthetic antiferromagnetic skyrmion bubbles, *Nat. Commun.* **10**, 5153 (2019).
- [12] J. Barker and O. A. Tretiakov, Static and Dynamical Properties of Antiferromagnetic Skyrmions in the Presence of Applied Current and Temperature, *Phys. Rev. Lett.* **116**, 147203 (2016).
- [13] W. Jiang, X. Zhang, G. Yu, W. Zhang, X. Wang, M. Benjamin Jungfleisch, J. Pearson, X. Cheng, O. Heinonen, K. L. Wang, Y. Zhou, A. Hoffmann, and S. te Velthuis, Direct observation of the skyrmion Hall effect, *Nat. Phys.* **13**, 162 (2017).
- [14] S. Woo, K. M. Song, X. Zhang, Y. Zhou, M. Ezawa, X. Liu, S. Finizio, J. Raabe, N. J. Lee, S.-I. Kim, S.-Y. Park, Y. Kim, J.-Y. Kim, D. Lee, O. Lee, J. W. Choi, B.-C. Min, H. C. Koo, and J. Chang, Current-driven dynamics and inhibition of the skyrmion Hall effect of ferrimagnetic skyrmions in GdFeCo films, *Nat. Commun.* **9**, 959 (2018).
- [15] M. Stier, W. Häusler, T. Posske, G. Gurski, and M. Thorwart, Skyrmion–Anti-Skyrmion Pair Creation by In-Plane Currents, *Phys. Rev. Lett.* **118**, 267203 (2017).
- [16] X. Zhang, Y. Zhou, and M. Ezawa, Magnetic bilayer-skyrmions without skyrmion Hall effect, *Nat. Commun.* **7**, 10293 (2016).
- [17] V. Baltz, A. Manchon, M. Tsoi, T. Moriyama, T. Ono, and Y. Tserkovnyak, Antiferromagnetic spintronics, *Rev. Mod. Phys.* **90**, 015005 (2018).
- [18] G. Yin, Y. Li, L. Kong, R. K. Lake, C. L. Chien, and J. Zang, Topological charge analysis of ultrafast single skyrmion creation, *Phys. Rev. B* **93**, 174403 (2016).
- [19] S. G. Je, H. S. Han, S. K. Kim, S. A. Montoya, W. Chao, I. S. Hong, E. E. Fullerton, K. S. Lee, K. J. Lee, M. Y. Im, and J. I. Hong, Direct Demonstration of Topological Stability of Magnetic Skyrmions via Topology Manipulation, *ACS Nano* **14**, 3251 (2020).
- [20] S. Rohart, J. Miltat, and A. Thiaville, Path to collapse for an isolated Néel skyrmion, *Phys. Rev. B* **93**, 214412 (2016).
- [21] T. Nishimura, M. Haruta, D. H. Kim, Y. Shiota, H. Iwaki, D. Kan, T. Moriyama, H. Kurata, and T. Ono, Fabrication of ferrimagnetic Co/Gd/Pt multilayers with structural inversion symmetry breaking, *J. Magnetism Soc. Jpn.* **44**, 9 (2020).
- [22] H. Yang, A. Thiaville, S. Rohart, A. Fert, and M. Chshiev, Anatomy of Dzyaloshinskii-Moriya Interaction at Co/Pt Interfaces, *Phys. Rev. Lett.* **115**, 267210 (2015).
- [23] H. Yang, O. Boulle, V. Cros, A. Fert, and M. Chshiev, Controlling Dzyaloshinskii-Moriya interaction via chirality dependent atomic-layer stacking, insulator capping and electric field, *Sci. Rep.* **8**, 12356 (2018).
- [24] M. Belmeguenai, J. P. Adam, Y. Roussigné, S. Eimer, T. Devolder, J. V. Kim, S. M. Cherif, A. Stashkevich, and A. Thiaville, Interfacial Dzyaloshinskii-Moriya interaction in perpendicularly magnetized Pt/Co/AlOx ultrathin films measured by Brillouin light spectroscopy, *Phys. Rev. B* **91**, 180405(R) (2015).
- [25] L. Caretta, M. Mann, F. Büttner, K. Ueda, B. Pfau, C. M. Günther, P. Helsing, A. Churikova, C. Klose, M. Schneider, D. Engel, C. Marcus, D. Bono, K. Bagschik, S. Eisebitt, and G. S. D. Beach, Fast current-driven domain walls and small skyrmions in a compensated ferrimagnet, *Nat. Nanotechnol.* **13**, 1154 (2018).
- [26] R. Streubel, C. H. Lambert, N. Kent, P. Ercius, A. T. N’Diaye, C. Ophus, S. Salahuddin, and P. Fischer, Experimental Evidence of Chiral Ferrimagnetism in Amorphous GdCo Films, *Adv. Mater.* **30**, 1800199 (2018).
- [27] J. Brandão, D. A. Dugato, M. V. Puydinger Dos Santos, and J. C. Cezar, Evolution of zero-field ferrimagnetic domains and

- skyrmions in exchange-coupled Pt/CoGd/Pt confined nanostructures: Implications for antiferromagnetic devices, *ACS Appl. Nano Mater.* **2**, 7532 (2019).
- [28] E. Burzo and D. Seitabla, On the induced cobalt moments in $(\text{Gd}_x\text{Y}_{1-x})\text{Co}_3$ compounds, *Solid State Commun.* **37**, 663 (1981).
- [29] I. A. Campbell, Indirect exchange for rare earths in metals, *J. Phys. F* **2**, L47 (1972).
- [30] C. Kittel, *Introduction to Solid State Physics*, 8th ed. (Wiley, Hoboken, NJ, 2004), p. 704.
- [31] J. H. Moon, S. M. Seo, K. J. Lee, K. W. Kim, J. Ryu, H. W. Lee, R. D. McMichael, and M. D. Stiles, Spin-wave propagation in the presence of interfacial Dzyaloshinskii-Moriya interaction, *Phys. Rev. B* **88**, 184404 (2013).
- [32] M. Kostylev, Interface boundary conditions for dynamic magnetization and spin wave dynamics in a ferromagnetic layer with the interface Dzyaloshinskii-Moriya interaction, *J. Appl. Phys.* **115**, 233902 (2014).
- [33] H. T. Nembach, J. M. Shaw, M. Weiler, E. Jué, and T. J. Silva, Linear relation between Heisenberg exchange and interfacial Dzyaloshinskii-Moriya interaction in metal films, *Nat. Phys.* **11**, 825 (2015).
- [34] A. A. Stashkevich, M. Belmeguenai, Y. Roussigné, S. M. Cherif, M. Kostylev, M. Gabor, D. Lacour, C. Tiusan, and M. Hehn, Experimental study of spin-wave dispersion in Py/Pt film structures in the presence of an interface Dzyaloshinskii-Moriya interaction, *Phys. Rev. B* **91**, 214409 (2015).
- [35] See Supplemental Material at <http://link.aps.org/supplemental/10.1103/PhysRevMaterials.6.084412> for additional supporting experimental details and simulations, which includes Refs. [49,50].
- [36] X. M. Cheng and D. J. Keavney, Studies of nanomagnetism using synchrotron-based x-ray photoemission electron microscopy (X-PEEM), *Rep. Prog. Phys.* **75**, 026501 (2012).
- [37] C. T. Chen, Y. U. Idzerda, H. J. Lin, N. V. Smith, G. Meigs, E. Chaban, G. H. Ho, E. Pellegrin, and F. Sette, Experimental Confirmation of the X-Ray Magnetic Circular Dichroism Sum Rules for Iron and Cobalt, *Phys. Rev. Lett.* **75**, 152 (1995).
- [38] J. Stöhr and S. Anders, X-ray spectro-microscopy of complex materials and surfaces, *IBM J. Res. Dev.* **44**, 535 (2000).
- [39] B. H. Frazer, B. Gilbert, B. R. Sonderegger, and G. De Stasio, The probing depth of total electron yield in the sub-keV range: TEY-XAS and X-PEEM, *Surf. Sci.* **537**, 161 (2003).
- [40] B. T. Thole, P. Carra, F. Sette, and G. van der Laan, X-ray Circular Dichroism as a Probe of Orbital Magnetization, *Phys. Rev. Lett.* **68**, 1943 (1992).
- [41] P. Carra, B. T. Thole, M. Altarelli, and X. Wang, X-Ray Circular Dichroism and Local Magnetic Fields, *Phys. Rev. Lett.* **70**, 694 (1993).
- [42] A. Vansteenkiste, J. Leliaert, M. Dvornik, M. Helsen, F. Garcia-Sanchez, and B. Van Waeyenberge, The design and verification of MuMax3, *AIP Adv.* **4**, 107133 (2014).
- [43] T. Ha Pham, J. Vogel, J. Sampaio, M. Vaňatka, J.-C. C. Rojas-Sánchez, M. Bonfim, D. S. Chaves, F. Choueikani, P. Ohresser, E. Otero, A. Thiaville, S. Pizzini, T. H. Pham, J. Vogel, J. Sampaio, M. Vaňatka, J.-C. C. Rojas-Sánchez, M. Bonfim, D. S. Chaves, F. Choueikani, P. Ohresser, E. Otero, A. Thiaville, and S. Pizzini, Very large domain wall velocities in Pt/Co/GdOx and Pt/Co/Gd trilayers with Dzyaloshinskii-Moriya interaction, *Europhys. Lett.* **113**, 67001 (2016).
- [44] R. Bläsing, T. Ma, S.-H. Yang, C. Garg, F. K. Dejene, A. T. N'Diaye, G. Chen, K. Liu, S. S. P. Parkin, A. T. N'Diaye, G. Chen, K. Liu, and S. S. P. Parkin, Exchange coupling torque in ferrimagnetic Co/Gd bilayer maximized near angular momentum compensation temperature, *Nat. Commun.* **9**, 4984 (2018).
- [45] V. M. Parakkat, K. R. Ganesh, and P. S. Anil Kumar, Tailoring Curie temperature and magnetic anisotropy in ultrathin Pt/Co/Pt films, *AIP Adv.* **6**, 056118 (2016).
- [46] C.-J. Lin, G. L. Gorman, C. H. Lee, R. F. C. Farrow, E. E. Marinero, H. V. Do, H. Notarys, and C. J. Chien, Magnetic and structural properties of Co/Pt multilayers, *J. Magn. Magn. Mater.* **93**, 194 (1991).
- [47] E. Stavrou and K. Röhl, Magnetic anisotropy in Gd/(FeCo) and Gd/Fe multilayers for high density magneto-optical recording, *J. Appl. Phys.* **85**, 5971 (1999).
- [48] E. Stavrou, R. Sbiaa, T. Suzuki, S. Knappmann, and K. Röhl, Magnetic anisotropy and spin reorientation effects in Gd/Fe and Gd/(FeCo) multilayers for high density magneto-optical recording, *J. Appl. Phys.* **87**, 6899 (2000).
- [49] R. Nakajima, J. Stöhr, and Y. U. Idzerda, Electron-yield saturation effects in L-edge x-ray magnetic circular dichroism spectra of Fe, Co, and Ni, *Phys. Rev. B* **59**, 6421 (1999).
- [50] O. S. Lutes, J. O. Holmen, R. L. Kooyer, and O. S. Aadland, Inverted and biased loops in amorphous Gd-Co films, *IEEE Trans. Magn.* **13**, 1615 (1977).